JOURNAL OF CATALYSIS 129, 457–472 (1991)

Effective Diffusivities in Catalyst Pellets: New Model Porous Structures and Transport Simulation Techniques

SEBASTIAN C. REYES AND ENRIQUE IGLESIA

Corporate Research Laboratories, Exxon Research and Engineering Company, Route 22 East, Annandale, New Jersey 08801

Received October 22, 1990; revised January 24, 1991

Compressed and sintered porous solids are simulated by random-loose aggregates of spheres that are distributed in size and partially overlapped to achieve the required porosity. The resulting porous networks closely capture the morphological details of diffusing channels within granular materials commonly used as catalyst supports. Effective diffusivities in these model solids are calculated by Monte Carlo techniques that allow the probing of representative regions of the void space throughout the Knudsen, transition, and molecular diffusion regimes. Simulated diffusivities and tortuosity factors are in excellent agreement with experimental observations. These simulations also allow the calculation of accurate pore-size distributions and of transition-region diffusivities, previously estimated by simple geometric arguments and by the Bosanquet approximation, respectively. Mean pore radii calculated from surface area (S) and porosity (Φ^A) data ($\bar{r}_p = 2\Phi^A/S$) closely resemble the exact values obtained in our simulations for compressed solids but less so for sintered materials. Our simulations show that tortuosity factors, when properly defined and calculated, are intrinsic properties of porous solids, and identical in the Knudsen and molecular diffusion regimes.

1. INTRODUCTION

Reactant and product transport through complex and often dynamic porous materials are essential requirements for stoichiometric and catalytic gas–solid reactions. Transport limitations frequently restrict the arrival of reactants to and the removal of products from reactive sites. They often control reaction rates and selectivity as well as the formation of deposits that modify the chemical reactivity and the pore structure.

Diffusivity measurements require testing of representative samples at conditions that avoid adsorption and diffusion on the pore surfaces (*1*). Data interpretation and extrapolation to reaction conditions or to related materials require detailed characterization of the pore structure and the use of an appropriate average pore radius (Knudsen diffusion regime) or of an equivalent capillary diffusivity (transition diffusion regime) (*2*). These difficulties are apparent in the wide range of tortuosities reported in the literature (*3, 4*).

Porous solids are traditionally described by capillary network models ranging from simple parallel arrangements of uniform cylinders to models of tortuous capillaries of varying size and orientation (Fig. 1a). These models do not include the effects of dead ends, pore branching, and fluctuating pore size. As a result, their use requires empirical tortuosity factors that incorporate not only the intrinsic geometric tortuosity of the pore structure, but also corrections for the inadequacies of the respective models. Bethe lattice networks (*2, 5*) of randomly interconnected capillaries distributed in size remove some of the limitations of earlier capillary bundle models (Fig. 1b). However, an equivalent connectivity is still required in order to account for the lack of lattice reconnections.

A priori estimates of effective diffusivities in porous solids require detailed descrip-

0021-9517/91 $3.00

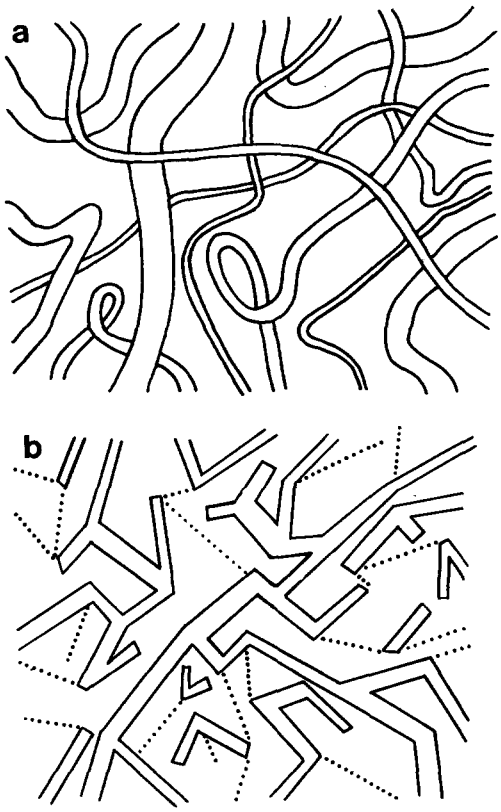

FIG. 1. (a) Schematic representation of pore network of unconnected capillaries. (b) Schematic representation of a pore network simulated with 3-coordinated Bethe lattice.

tions of important geometric and topological properties, such as local fluctuations in pore size, shape, and connectivity, that cannot be directly measured with available characterization techniques. Here, we report new Monte Carlo simulation procedures for the creation of random assemblages of microspheres and for the estimation of effective diffusivities in such model porous structures. Our approach incorporates many of the pioneering features of the sphere-packing models of Evans and coworkers (*6*). We extend their work significantly by creating pore structures that more closely resemble many porous materials used as catalyst supports. We also introduce a new and efficient simulation procedure that permits the sampling of representative regions of the pore structure in the molecular and transition diffusion regimes.

2. DIFFUSION IN POROUS SOLIDS

The mechanism by which molecules diffuse within pores depends on the ratio of the characteristic pore dimension (r_p) to the mean free path (λ). For $\lambda \ll r_p$ and $\lambda \gg r_p$, transport is dominated by molecule–molecule and molecule–surface collisions, respectively. These mechanisms are known as bulk and Knudsen regimes; their respective diffusivities are given by

$$D_b = \lambda\nu/3 \quad \text{(bulk)} \tag{1}$$

$$D_k = 2r_p\nu/3 \quad \text{(Knudsen)}, \tag{2}$$

where ν is the mean molecular velocity (*8*). Equation (2) is strictly valid for long cylindrical pores. In the transition diffusion regime, where λ and r_p values are similar, the Bosanquet equation (*9*) is commonly used:

$$D_t = [D_b^{-1} + D_k^{-1}]^{-1}; \tag{3}$$

again, it is rigorously valid only for diffusion within a long cylindrical pore. The calculation of effective diffusivities in a porous solid requires that we modify the above equations in order to account for the spatially changing size, shape, and branchiness of the pores. In addition, corrections must be made for the presence of solids that take up volume otherwise available for transport. Thus, effective diffusivities in porous solids (D^e) are conventionally calculated by

$$D^e = \Phi^B\bar{D}/\tau, \tag{4}$$

where Φ^B is the accessible porosity contained within interconnected backbones, $\bar{D}$ is an equivalent diffusivity averaged over the pore-size distribution (accounting for contributions of pores of different size), and τ is the tortuosity factor.

The tortuosity factor measures the increased diffusion pathlength imposed by the presence of solid obstacles. It is, therefore, an intrinsic geometric property of the solid; it should be independent of the diffusion mechanism. In practice, however, tortuosi-

ties frequently become adjustable parameters that compensate for inadequacies in evaluating the various terms of the defining Eq. (4). First, the equivalent diffusivity $\bar{D}$ does not take into account the connectivity of the pore space. Also, poorly inferred (from adsorption or porosimetry data) cylindrical pore radii are used to describe the irregular shape of the pore cavities. Moreover, total accessible porosity, Φ^A, rather than backbone porosity, is commonly used in Eq. (4). The backbone porosity, Φ^B, is the proper choice because unlike Φ^A, it excludes dead ends that do not contribute to transport (*2, 5*). Yet, Eq. (4) has been widely used.

In the bulk regime, diffusion does not depend on pore size, and $\bar{D}$ is simply replaced by D_b. In the Knudsen and transition regimes, the calculation of $\bar{D}$ requires that we include the contribution from pores of different sizes. Two approaches have traditionally been used. The first, proposed by Satterfield and co-workers (*3*), estimates an average pore radius $\bar{r}_p$ from experimentally measured accessible porosity (Φ^A) and surface area per unit volume (S):

$$\bar{r}_p = 2\,\Phi^A/S. \tag{5}$$

This average pore radius is then used to calculate D_t as a surrogate for $\bar{D}$. The second approach, proposed by Wang and Smith (*10*), estimates $\bar{D}$ by averaging D_t over the entire pore-size distribution $f(r)$:

$$\bar{D} = \int D_t(r) f(r)\, dr. \tag{6}$$

Thus, both approaches incorporate the role of fluctuating or distributed pore sizes only in an average sense and without explicitly accounting for pore interconnections and shape irregularity. Therefore, these approaches often lead to tortuosity values much greater than actual geometric pathlengths (*12*) and sensitive to temperature and pressure (*10, 11*). These tortuosity factors include not only an increased diffusion pathlength, but other factors that compensate for the inappropriate use of accessible rather than backbone porosity and for inaccuracies in the $\bar{D}$ estimates required in Eq. (4).

3. SIMULATION PROCEDURES

3.1 Pore Structure Model

Typical catalyst support pellets often consist of macroscopic aggregates of touching or partially overlapping microspheres with diffusion channels defined by the voids between them. Scanning electron micrographs of commonly used silica (Shell S980B), alumina (Linde, RT-12), and titania (Degussa P25) support structures are shown in Fig. 2. Two major steps are involved in the fabrication of these materials. The first is the formation of loosely bound assemblages of spherical microparticles by sol-gel processes. The second is the porosity (and mechanical strength) control by compression, extrusion, or thermal sintering. The internal surface area and characteristic pore dimensions of the resulting material are determined by the size of the starting microspheres and by the degree of compression and sintering.

In order to simulate these porous structures, we start our computer simulations by packing spheres in three dimensions. We create macroscopic assemblages of spheres under a gravitational field using packing rules consistent with loading procedures in slowly settled packed beds (*7*). The spheres can be monosize or varied in size and nonporous or themselves consisting of clusters of yet smaller spheres; they are placed randomly or at specified positions within a macroscopic aggregate. These packing procedures leads to random-loose porous structures that contain key geometrical and topological features typical of diffusing channels within porous solids. These packings are subsequently modified by partial overlap and random removal of spheres in order to simulate porosity changes caused during compression or sintering. Compression is simulated by increasing the radii of the spheres to an extent prescribed by a distribution function until a specified porosity is attained. Thermal sintering is simulated by randomly removing spheres from

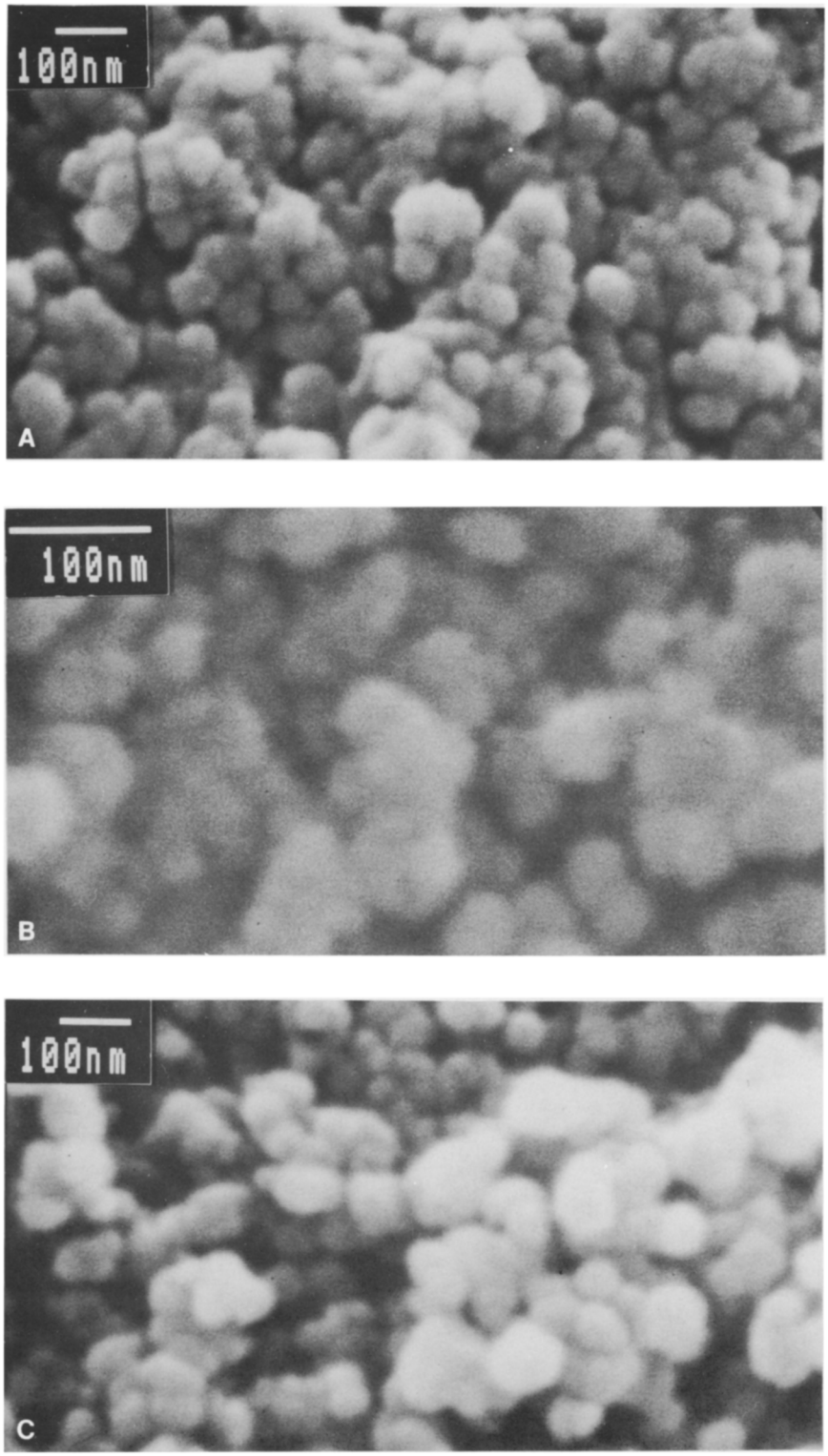

FIG. 2. Scanning electron micrographs of commonly used catalyst support structures (A) SiO_2; (B) Al_2O_3; (C) TiO_2.

an aggregate previously subjected to significant overlap (porosity equal to 0.05). While neither of these routes describes the physical processes involved in actual fabrication procedures, their resulting pore volume characteristics are remarkably similar to those found in compressed and sintered structures. Therefore, in what follows, we refer to these model materials as "compressed" and "sintered" solids, respectively. Cross-sectional views of three-dimensional simulated structures are shown in Fig. 3. Three-dimensional views of actual and simulated structures are shown in Figs. 4 and 5.

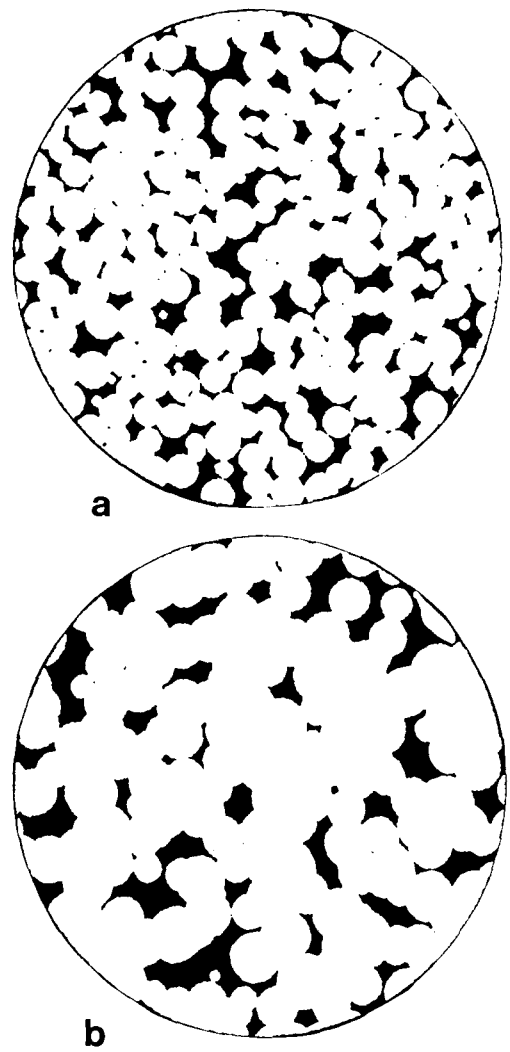

FIG. 3. Cross-sectional views of three-dimensional simulated porous solids. (a) Compressed solid. (b) Sintered solid.

3.2 Diffusion Simulations

Effective diffusivities are calculated by monitoring the displacement of molecules within the simulated three-dimensional porous structures. No assumptions are needed about the size, shape, and connectivity of the pores; only the sphere-size distribution and the extent of overlap (porosity) are required. These structural features are naturally built into the simulated porous structure. Molecules are placed at random locations within the voids of the model solid sample. They move in discrete steps within the solid by colliding with the solid surfaces and with other molecules. The distances travelled between molecular collisions are described by a logarithmic distribution of free paths that arises from kinetic theory (*6*). For a given solid, the type and frequency of the collisions depend on the mean free path. At higher pressures (i.e., smaller mean free paths), molecular collisions are more likely to occur. As the mean free path increases (lower pressures), molecules collide against solid surfaces with increasing probability. Upon collision with solid surfaces, molecules adsorb momentarily and then desorb in directions prescribed by a cosine law. The effective diffusion coefficient, D^e, is then calculated from the Brownian motion relation,

$$\langle R^2 \rangle = 6\, D^e t, \qquad (7)$$

where $\langle R^2 \rangle$ is the mean-squared displacement and t is the elapsed time. The correct application of Eq. (7) requires the proper selection of elapsed time (and thus of volume in the probed region) and of the number of molecules used to calculate $\langle R^2 \rangle$. In effect, accurate simulations require that molecules probe representative regions of the pore structure. Thus, both long times and large number of tracer molecules must be used. A few thousand (1000–2000) molecules with average displacements greater than about 10 microsphere diameters were

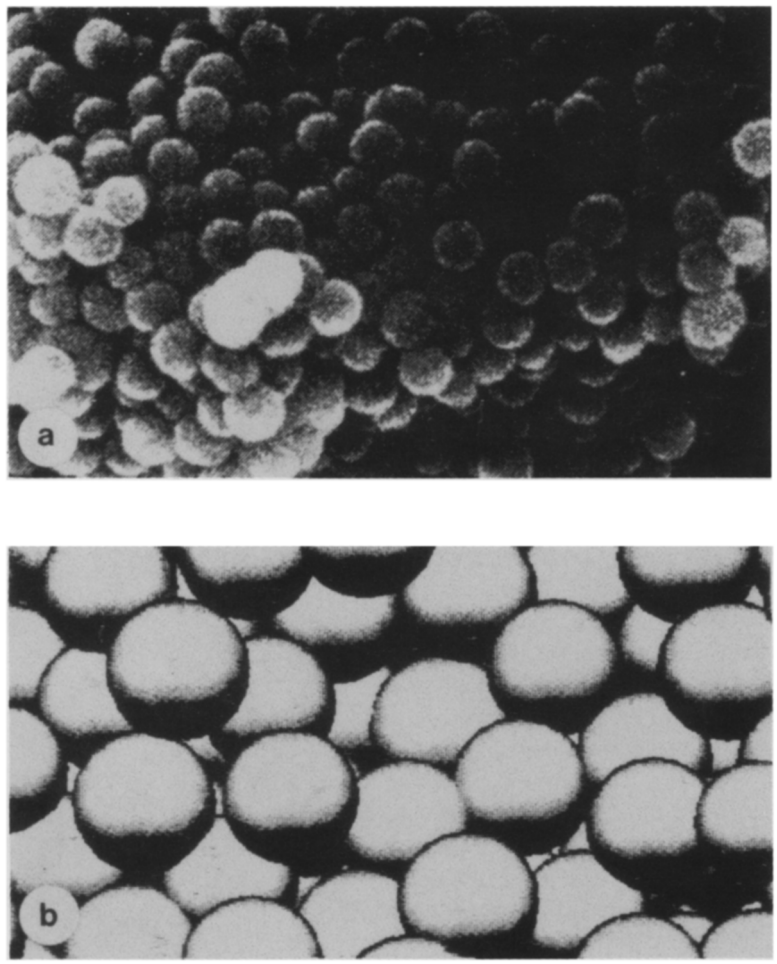

FIG. 4. Three-dimensional views of actual and simulated porous structures. (a) SEM of compressed silica microspheres. (b) Simulated compressed solid.

typically required for accurate and reproducible diffusivity calculations.

Computational time is proportional to the number of discrete steps required in each simulation. As schematically shown in Fig. 6, the number of steps required to cover a given distance increases rapidly as the diffusion mechanism progresses from Knudsen to transition and bulk regimes (i.e., as the λ/r_p ratio decreases). Molecules with small mean free paths require a large number of collisions in order to cover representative regions of the solid. Thus, we found that only Kundsen diffusivities (large λ) could be calculated in a reasonable computing time. Transition and bulk diffusivity estimates require more efficient simulation techniques.

Molecular collisions control transport rates in the transition and bulk diffusion regimes; under those conditions, molecules probe the presence of the wall only when near a solid surface. This suggested a hybrid discrete/continuum simulation procedure that averages Brownian motion behavior away from solid surfaces while monitoring discrete steps near solid surfaces. This is

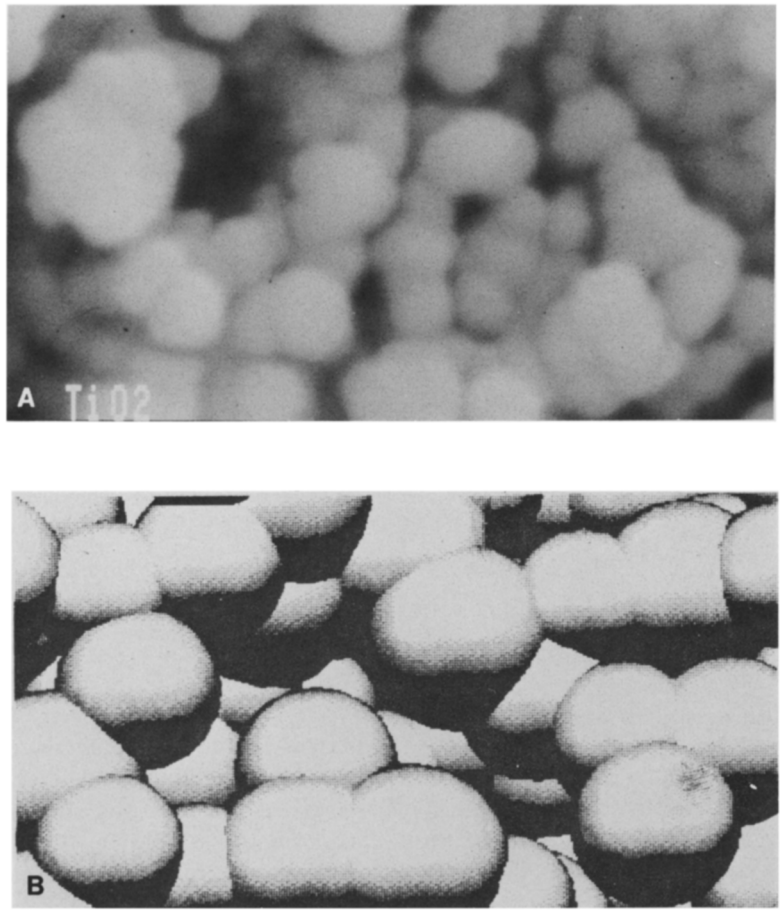

FIG. 5. Three-dimensional views of actual and simulated porous structures. (A) SEM of sintered titania microspheres. (B) Simulated sintered solid.

schematically shown in Fig. 7. Molecules advance through the pore space by a sequence of events that depends on whether the molecule is inside or outside a prescribed imaginary boundary layer, δ, that surrounds all solid surfaces. Within this boundary layer, only discrete random walks are allowed. Outside this boundary layer, molecules are allowed to advance in a single event (consisting of many individual collisional events) to a random point on the surface of the imaginary sphere that makes point contact with the nearest solid surface. The elapsed time for this event corresponds to the first passage time (FPT); it is obtained from the solution of the appropriate continuum diffusion equation governing the Brownian motion of molecules in free space (*13*). Thus, in our case, the FPT corresponds to the time taken for a molecule to reach the surface of an imaginary sphere of radius R for the first time. These times are distributed according to a probability distribution function whose mean value is $R^2/6D_b$. The boundary layer is required because FPT spheres smaller than a given size $R = N\lambda$ (N is the number of mean free paths) lack a sufficient number of discrete steps for the valid application of the continuum diffusion equation. The value of the boundary layer

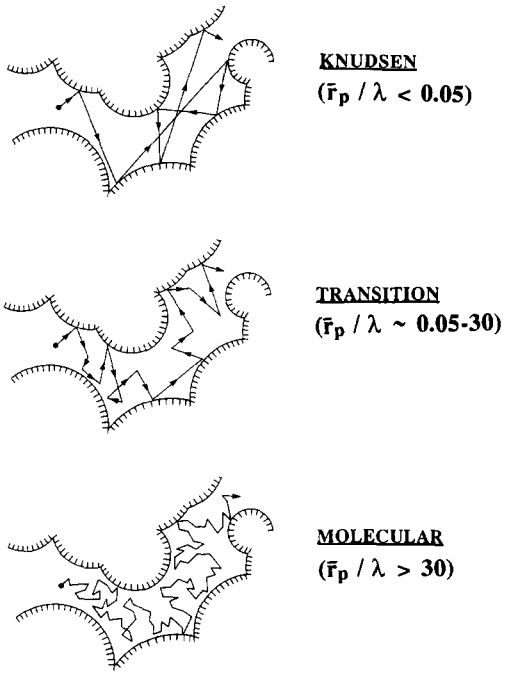

FIG. 6. Diffusion mechanisms in constrained voids.

thickness is chosen as an effective compromise between accuracy and speed of the simulations; it equals the radius of the smallest imaginary sphere allowed in the FPT calculations.

4. RESULTS AND DISCUSSION

4.1 Knudsen Diffusion Regime

Knudsen diffusion is the dominant transport mechanism when the mean free path of the diffusing molecules is much greater than the local pore dimensions. The Knudsen simulations consist of monitoring the displacement of tracer molecules as they repeatedly collide with the solid surfaces. Therefore, during the course of these simulations, one can also determine the pore-size distribution of the solid by simply recording the distances traversed by the molecules between successive surface collisions.

Knudsen diffusivities of compressed and sintered solids were calculated using Eq. (7). These results are presented in Fig. 8 as

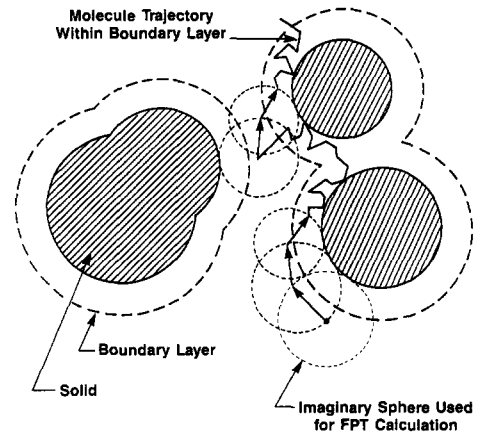

FIG. 7. Schematic representation of hybrid discrete/continuum simulation of molecular displacements within random pore structures.

normalized diffusivities. Normalized diffusivities are defined as

$$E = D^e/\bar{D}_k, \tag{8}$$

where $\bar{D}_k$ is the equivalent Knudsen diffusivity corresponding to the average pore radius calculated from the simulation procedure. Figure 8 shows that normalized diffusivities increase with increasing porosity but are remarkably independent of the porosity destruction mechanism (compression or sintering). The dependence of E on Φ is typical of percolating solids (*2*, *5*). A

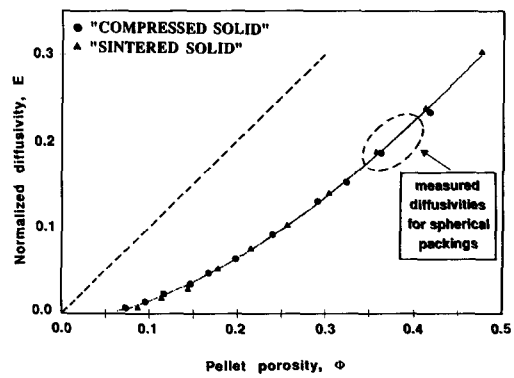

FIG. 8. Normalized effective Knudsen diffusivities in simulated compressed and sintered porous solids.

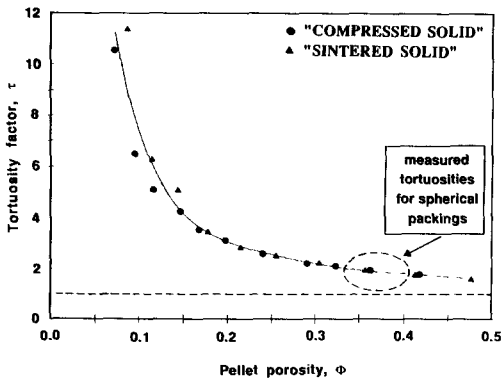

FIG. 9. Tortuosity factors in simulated compressed and sintered porous solids.

threshold porosity, below which no diffusion is possible, is clearly observed when the fraction of voids reaches about 0.05.

Although not required in the effective diffusivity calculations, a tortuosity factor can be obtained by combining Eqs. (4) and (8). The resulting geometric tortuosities ($\tau = \Phi^B/E$) are shown in Fig. 9 as a function of porosity. They depend weakly on porosity for $\Phi > 0.2$ but increase rapidly with decreasing porosity of $\Phi < 0.2$ because of the increased isolation of void volume in inaccessible and non-conducting dead-end regions. Tortuosities are similar for compressed and sintered solids. At very low porosities ($\Phi < 0.20$), sintered solids show slightly higher tortuosities, consistent with the higher probability of dead ends and of pore volume isolation during the sintering process.

Calculated pore-size distributions (normalized on a pore volume basis) for compressed and sintered solids are shown in Fig. 10 for various porosity values. These distributions resemble those typically obtained from mercury porosimetry and nitrogen adsorption experiments on porous materials. In our simulations, however, we do not assume a pore geometry or connectivity. Pore sizes reflect the characteristic distances that molecules actually travel between successive collisions with neighboring pore surfaces. Sintered solids have larger pores for a given porosity because large voids are created as neighboring spheres coalesce.

Tortuosity factors (τ) and normalized diffusivities (E) in compressed and sintered solids with a given porosity are very similar (Figs. 8 and 9), in spite of the different pore generation processes in the two types of solids. These results suggest that effective Knudsen diffusivities can be estimated a priori for random assemblages of microspheres by properly measuring a mean pore radius ($\bar{r}_p$). An expression for the effective diffusivity can be obtained by combining Eqs. (2) and (8):

$$D^e = \left(\frac{2}{3}\nu\bar{r}_p\right) \cdot E. \tag{9}$$

Thus, if E is a known function of porosity, such as that described by Fig. 8, only a measurement of $\bar{r}_p$ is additionally required. In principle, pore-size distributions can be obtained by porosimetry or adsorption methods. In practice, pore sizes inferred from these techniques require simplified pore structure models and are thus subject to interpretation errors.

Mean pore radii can also be obtained from Eq. (5). This equation requires only porosity and surface area measurements that are less prone to interpretation errors. Both properties (S and Φ^A) are also readily calculated for simulated compressed and sintered model structures. Figure 11 compares the mean pore radii calculated from Eq. (5) with the correct values obtained from the diffusivity simulations. We conclude that Eq. (5) gives an accurate value for the mean pore radius of compressed solids. Its use for sintered solids is less accurate, but the maximum error is less than 25%. These results strongly support the use of Eqs. (5) and (9) and of the results in Fig. 8 in order to estimate effective Knudsen diffusivities, because potential errors in $\bar{r}$ and D^e estimates (<25%)

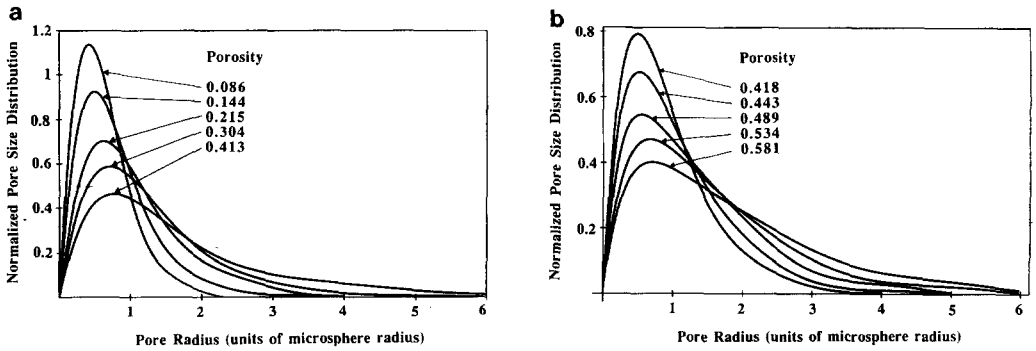

FIG. 10. Pore-size distributions in simulated solids. (a) Compressed solids. (b) Sintered solids.

are much smaller than those reported in experimental D^e and τ measurements.

4.2 Simulated and Experimental Knudsen Diffusivities

Huizenga and Smith (*14*) have reported diffusivity measurements in the Knudsen regime for porous solids formed by compressing narrowly distributed silica microspheres. We have compared our simulation results with their experimental values. The first step in the simulation consists of assembling representative samples of microspheres obeying their experimentally measured size distributions. The aggregates were subsequently coalesced to achieve their experimental porosities (compressed solids). Finally, Monte Carlo simulations were used to evaluate the effective Knudsen diffusivities.

Simulated (solid lines) and experimental (symbols) diffusivities for H_2, He, N_2, and Ar in six different solids are compared in Fig. 12. The solids consisted of microspheres of varying radii, ranging from 52 to 305 nm, and with porosities ranging from 0.331 to 0.385. The predicted diffusivities are in excellent agreement with the experimental values, demonstrating the adequate representation of the solid as well as the validity of our diffusion simulation procedure.

4.3 Transition and Bulk Diffusion Regimes

In the transition and bulk diffusion regimes, the number of discrete steps needed to probe representative solid regions is extremely large and we require the hybrid dis-

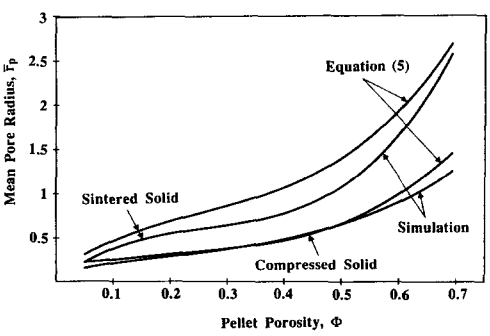

FIG. 11. Mean pore radii as a function of porosity for simulated compressed and sintered porous structures.

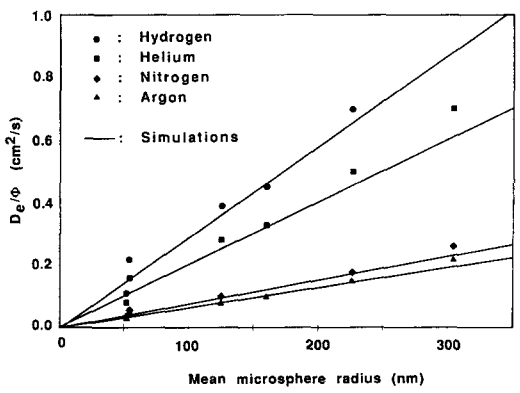

FIG. 12. Comparison of experimental (*14*) and simulated Knudsen diffusivities.

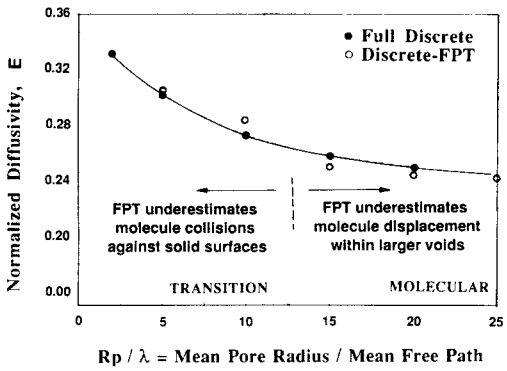

FIG. 13. Comparison of hybrid discrete/continuum versus full discrete simulation in transition/molecular diffusion regimes.

crete/continuum approach described in Section 3.2. This technique introduces some error by using the solution of Brownian motion in unbounded space (continuum diffusion equation) to approximate the random motion within a finite imaginary sphere (with radius $N\lambda$, $N \gg 1$).

The diffusivity estimates obtained by the hybrid simulation procedure are compared with those of exact discrete simulations (i.e., without FPT approximations) in Fig. 13. A model porous solid composed of nonoverlapping monosize spheres (radius r_s) having a porosity of 0.417 and a mean pore radius of $0.499r_s$ was used in the comparison. The $\bar{r}_p/\lambda$ ratio was varied by changing λ while maintaining the structure ($\bar{r}_p$) unchanged. Normalized diffusivities are defined as

$$E = D^E/\bar{D}_t, \tag{10}$$

where $\bar{D}_t$ is evaluated at λ and $\bar{r}_p = 0.499r_s$ using Eq. (3). Figure 13 shows that a boundary layer thickness of five mean free paths ($\delta = 5\lambda$) adequately reproduces the results of the full discrete simulations while significantly reducing computing time. The application of FPT approximations to imaginary spheres with radii less than about 5λ (i.e., boundary layer equal to 5λ) results in fast but inaccurate diffusivity estimates. In contrast, FPT simulations for boundary layers greater than about 5λ demand excessive use of discrete step-by-step monitoring of collisional events without significantly improving the accuracy of the diffusivity estimates.

The hybrid technique (with a boundary layer thickness of 5λ) was used to estimate diffusivities in all diffusion regimes for loosely packed non-overlapped solids ($\Phi = 0.417$). The $\bar{r}_p/\lambda$ ratio was varied from 0.01 to 70 by varying λ only. The results are shown in Fig. 14 in terms of a tortuosity factor, defined following Eq. (4), as

$$\tau = \Phi^B \bar{D}_t/D^e, \tag{11}$$

with the Bosanquet equation for $\bar{D}_t$ [Eq. (3)] replacing the equivalent diffusivity $\bar{D}$. Figure 14 shows that at both extremes in $\bar{r}_p/\lambda$, where $\bar{D}$ is rigorously given by D_k or D_b, the tortuosity approaches similar values (about 1.8). This clearly demonstrates the consistency of the simulation technique in accurately calculating effective diffusivities throughout all diffusion regimes. As already discussed, the geometric tortuosity is an intrinsic property of the porous structure that, if properly defined, is independent of the diffusion regime. The deviations at intermediate values of $\bar{r}_p/\lambda$ reflect the inadequacy of the Bosanquet equation in describing transition diffusion coefficients in an ensemble of non-cylindrical pores that vary in size, shape, and connectivity. The Bosanquet

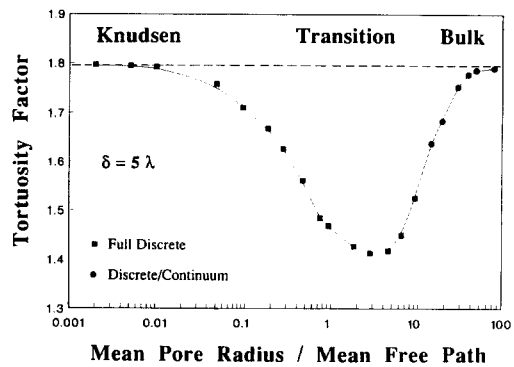

FIG. 14. Tortuosity factor as a function of mean pore radius/mean free path ratio for a model porous solid having a porosity of 0.417.

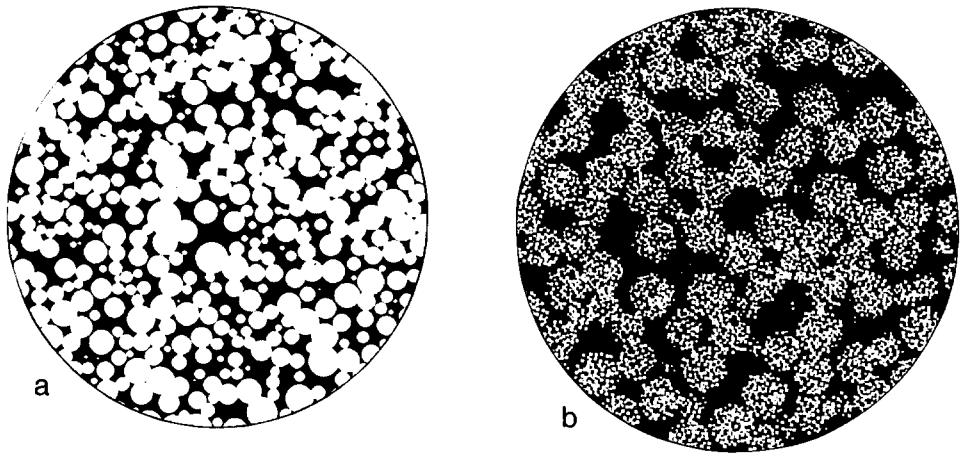

FIG. 15. Cross-sectional views of three-dimensional aggregates of multisize spheres. (a) Gaussian size distribution. (b) Segregated spatial distribution.

equation underestimates diffusivities (maximum error ~20% at $\bar{r}_p/\lambda = 3$), suggesting that diffusing molecules are able to "detect" and use neighboring larger pore openings in parallel with the diffusing channels, instead of following the strictly sequential mechanism implied by the Bosanquet equation.

4.4 Knudsen Diffusivities in Aggregates of Multisize Spheres

Here, we use packing procedures for the generation of random-loose aggregates of multisize spheres and for subsequent diffusion simulations in these structures. Spheres of size prescribed by a distribution function (e.g., Gaussian, bidisperse, or continuous) are located within pellets by following the procedures described in Section 3.1. Then, porosity is adjusted by partial overlapping of such spheres and effective diffusivities are calculated in the Knudsen diffusion regime.

Our procedures are capable of producing aggregates with arbitrary sphere-size distributions. Here, we illustrate Gaussian distributions in which the individual spheres are either randomly located (Fig. 15a) or segregated within a macroscopic aggregate (Fig. 15b). The latter lead to "bimodal" pore structures; they consist of aggregates of small spheres of mean diameter d_1 located within larger spherical voids of mean diameter d_2, that are themselves distributed randomly within a macropellet of diameter D ($D \gg d_2$). Figure 15 shows cross-sectional views of these two simulated solid structures. The structure shown in Fig. 15a was obtained by randomly packing and subsequently overlapping spheres obeying a Gaussian distribution with a mean sphere radius r_s and a standard deviation (σ) of $0.25r_s$; the distribution was truncated at $r_s \pm 3\sigma$. The segregated solid (Fig. 15b) was obtained by inserting aggregates of small spheres (mean diameter $d_1 = 0.1\ d_2$) within the voids left by the removal of large spheres (micropellets) from a previously assembled macroscopic aggregate (macropellet). These two types of model solids resemble those typically found in many catalyst support pellets.

The structural (pore-size distribution) and diffusive properties of Gaussian porous solids are analyzed by varying the breadth σ of the sphere-size distribution. Effective Knudsen diffusivities and associated mean pore radii are shown in Table 1. These results show that normalized effective diffusivities [E, Eq. (8)] are largely unaffected by increasing σ from 0 (monosize) to $1.5r_s$ (a

TABLE 1

Mean Pore Sizes and Knudsen Diffusivity Factors for Gaussian Non-overlapping Solids

σ	Φ	S^a	E	$\bar{r}_p{}^b$	$\bar{r}_p$-Ratio^c
0	0.417	1.744	0.233	0.499	0.958
0.33	0.412	1.748	0.233	0.496	0.950
0.50	0.407	1.768	0.235	0.478	0.963
0.67	0.405	1.788	0.228	0.469	0.966
0.83	0.402	1.802	0.232	0.468	0.953
1.00	0.400	1.820	0.230	0.462	0.951
1.50	0.397	1.870	0.229	0.447	0.950

[a] Units of reciprocal mean sphere radius.

[b] From diffusivity simulation, units of mean sphere radius.

[c] Ratio of mean pore radius calculated from Eq. (5) to that obtained from diffusivity simulations.

broad distribution). The mean pore radii calculated by the diffusivity simulations decrease as we increase the breadth of the size distribution. This is a consequence of the compaction effect that is clearly reflected in a slight decrease in void fraction as σ increases. We observe, however, that mean pore radii estimated from Eq. (5) also decrease slightly as σ increases; their values are slightly lower than those calculated in the simulation procedure (ratio ~0.95–0.96) but nearly independent of the breadth of the Gaussian distribution. Therefore, we conclude that Eq. (5) provides an accurate estimate of the mean pore radius required for calculations of effective Knudsen diffusivities in random assemblages of Gaussianly distributed spheres. As previously found for single-size spheres, these estimates remain accurate as we decrease the porosity by overlapping spheres in compressed solids, but significantly less so in sintered solids.

The corresponding effective Knudsen diffusivities and mean pore radii for segregated solids are shown in Table 2; the solids consist of non-overlapping monosize spheres having total porosities in the range 0.682 to 0.660. The latter value is attained for $d_1/d_2 \leq 0.1$ and reflects a contribution from both small ($\Phi = 0.243$) and large ($\Phi = 0.417$) voids in the solid. As expected, the calculated mean pore radius ($\bar{r}_p$) decreases as we decrease the sphere-size ratio (d_1/d_2) because molecules probe a pore structure that contains increasing amounts of smaller pores. The increased porosity due to micropellet voids results in higher effective diffusivities D_k^e than in the monosize case ($d_1/d_2 = 1$). This enhancement, however, disappears as the size ratio decreases because the smaller pores eventually contribute little to net macroscopic transport throughout the macropellet. For example, the transport enhancement by micropellet pores is less than 3% for a size ratio of 0.1.

Mean pore radii calculated from diffusivity simulations and from Eq. (5) are in close agreement for segregated pore structures (Table 2). However, neither is appropriate for the calculation of the equivalent diffusion coefficients (D_k) that are required for effective diffusivity estimates (Eq. (8)). Net macroscopic transport occurs increasingly within the larger voids between micropellets as the size ratio decreases. Thus, while probe molecules sample the entire void space and reveal the true pore-size distribu-

TABLE 2

Mean Pore Sizes and Effective Knudsen Diffusivities of Bimodal Non-overlapping Solids

d_1/d_2	Φ	S^a	D_k^e/ν^b	$\bar{r}_p{}^c$	$\bar{r}_p$-Ratio^d	Y^e
1	0.417	1.744	0.117	0.499	0.958	1.00
0.25	0.682	3.820	0.185	0.369	0.968	1.57
0.20	0.670	4.950	0.151	0.776	0.981	1.29
0.166	0.665	6.060	0.140	0.226	0.971	1.20
0.125	0.663	8.087	0.123	0.167	0.982	1.05
0.10	0.660	10.197	0.121	0.132	0.981	1.03

[a] Units of reciprocal of mean sphere radius.

[b] Units of mean sphere radius.

[c] From diffusivity simulations, units of mean sphere radius.

[d] As (3) in Table 1.

[e] Enhancement factor; ratio of effective Knudsen diffusivity D_k^e for a given ratio to that for a ratio of 1.

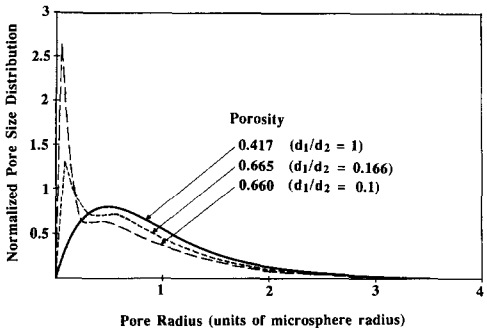

FIG. 16. Pore-size distributions in simulated bimodal solids.

tion within a macroscopic sample, they cover macroscopic distances predominantly while traveling through larger voids. In the limit of small size ratios, typical of catalyst support pellets, our simulation measures transport exclusively through the larger voids without any significant use of the smaller pores within micropellets.

Our simulation procedure samples the entire pore structure and allows the calculation of pore-size distributions irrespective of size ratio. Figure 16 clearly shows the presence of a bimodal pore-size distribution consisting of pore structures within and between micropellet aggregates. However, an important conclusion of our simulations is that the additional porosity within micropellets does not contribute to net macroscopic transport for size ratios less than about 0.1.

Segregated bimodal pore structures pose unique problems in the estimation of proper effective diffusivities needed in catalytic reaction rate calculations. First, for macroscopic transport, only the porosity between micropellets and its associated tortuosity factor are required in Eq. (4). Thus, Eq. (5) no longer describes the mean pore radius required in equivalent diffusivity estimates, because total surface area and porosity are measured throughout the solid and do not solely reflect the properties of the conducting backbone channels between micropellets. When possible, we can overcome these difficulties by an experimental or mathematical deconvolution of the pore-size distribution, which distinguishes the porosity and surface area contained within the two pore systems. Then, Eq. (5) remains valid in the limit of $d_1/d_2 < 0.1$; porosity and surface area between micropellets can be used to calculate effective diffusivities across the macroscopic pellet, while those within the smaller voids are used to calculate micropellet diffusivities. The latter become crucial for transport-limited reactions because a predominant fraction of the surface area, and thus of the stoichiometric or catalytic function, is contained within such micropellets. The interplay of macropellet (D_M) and micropellet (D_m) diffusivities in the design of segregated pellets for transport-limited catalytic reactions is the subject of the last section in this report and of on-going research in our laboratory (*15*).

4.5 Bimodal Pore-Size Distributions and the Design of Catalyst Pellets

The rate of a first-order catalytic reaction within a segregated macropellet of radius R_M, and consisting of micropellets of radius R_m, is given by

$$\text{Rate} = 4\pi R_M C_0 D_m(\psi_M \coth \psi_M - 1) \quad (12)$$

with Thiele moduli defined as

$$\psi_M^2 = \frac{S_M R_M^2}{R_m}\left(\frac{D_m}{D_M}\right)(\psi_m \coth \psi_m - 1) \quad (13)$$

$$\psi_m^2 = \frac{k S_m R_m^2}{D_m}, \quad (14)$$

where C_0 is the reactant concentration at the pellet surface, k is the reaction rate constant, and S_m and S_M are the micropore and macropore surface areas per unit volume, respectively. These expressions show that reaction rates in a transport-limited segregated pellet depend on both the micropellet (D_m, S_m) and the macropellet (D_M, S_M) diffusivities and surface areas.

The complex interplay between the radii and surface area within a micropellet (controlled by the size and degree of overlap

of the composing microspheres) and those between the micropellets (defined by their size and extent of overlap) is clearly illustrated by Eqs. (12)–(14). Large micropores, although desirable for transport, occupy volume otherwise available for catalytic solid (i.e., D_M increases but S_m decreases). In contrast, the small micropores that provide most of the catalytic surface areas slow down transport (i.e., S_m increases but D_m decreases). These competing effects clearly suggest that reaction rates in bimodal segregated structures can benefit significantly from optimal selection of characteristic micropore and macropore dimensions. The optimization of support structural properties for rate and selectivity improvements in catalytic reactions is discussed in detail elsewhere (*15*).

5. CONCLUSIONS

We describe here new methods for the generation of model porous structures that realistically capture morphological features of many catalyst supports. These structures consist of random-loose aggregates of microspheres, appropriately overlapped to describe porosites experimentally obtained by compression or sintering. Effective Knudsen diffusivity calculations within these porous structures are in excellent agreement with reported experimental values. The (true) mean pore radii in these porous solids differ slightly from those given by the conventional approximation ($2\Phi^A/S$) used to estimate equivalent diffusivities within cylindrical pores.

We also report here the first application of a new simulation technique that allows representative sampling of the pore structure in the molecular and transition diffusion regimes. This simulation technique combines monitoring of discrete collision events near solid surfaces with approximate averaging techniques (first passage time theory) in void regions away from them. Effective diffusivities simulations thus become possible for the entire range of diffusion mechanisms. Our results demonstrate that the geometric tortuosity of random-loose aggregates of microspheres is about 1.8 in both the Knudsen and bulk diffusion regime. Deviations from this value in the transition diffusion region (<20%) result from inaccuracies in the application of the Bosanquet equation to calculate diffusion coefficients within equivalent cylindrical pores in the transition diffusion region.

Mean pore radii and Knudsen diffusion properties in aggregates of multisize spheres demonstrate the importance of size distribution and of spatial segregation of the bimodal pore space. For spheres obeying a Gaussian distribution of sizes, the true mean pore radius required in the calculation of an equivalent diffusivity is completely characterized by the mean, and independent of the breadth, of the distribution. For bimodal pore structures, diffusion occurs in both micropores and macropores, but the latter becomes dominant as the ratio of micropore and macropore radii decreases.

On-going studies address the extension of the models to include surface diffusion, surface-catalyzed reactions, separations of mixtures within porous inorganic membranes, and relaxation phenomena (e.g., Xenon-129 nuclear magnetic resonance (*16*)) within microporous solids.

APPENDIX

Nomenclature

C_0: reactant concentration at pellet surface
D: pellet diameter
D_b: bulk diffusivity
D_k: Knudsen diffusivity
D_k^e: effective Knudsen diffusivity
D_m: effective micropellet diffusivity
D_M: effective macropellet diffusivity
D_t: transition diffusivity
D^e: effective diffusivity
$\overline{D}$: equivalent average diffusivity
$\overline{D}_k$: average Knudsen diffusivity
$\overline{D}_t$: average transition diffusivity
d_1, d_2: mean diameter of microspheres

E: normalized effective diffusivity
$f(r)$: pore-size distribution
k: reaction rate constant
N: number of mean free paths
R: radius of imaginary sphere
R_m: radius of micropellet
R_M: radius of macropellet
r_p: pore radius
r_s: microsphere radius
$\bar{r}_p$: mean pore radius
$\langle R^2 \rangle$: mean-squared displacement
S: surface area per unit volume
S_m: surface area per unit volume in micropellets
S_M: surface area per unit volume in macropellets
t: time
Y: enhancement ratio, defined in Table 2

Greek Symbols

λ: mean free path
δ: boundary layer thickness
ν: mean molecular velocity
σ: standard deviation
τ: tortuousity factor
Φ: pellet porosity
Φ^A: accessible porosity
Φ^B: backbone porosity
ψ_m: Thiele modulus in micropellets
ψ_M: thiele modulus in macropellets

ACKNOWLEDGMENTS

We gratefully acknowledge discussions with Professor Yee C. Chiew (Rutgers University) regarding the application of first-passage time concepts to diffusion in porous solids. We also thank Mr. Scott Ferguson for generating the two- and three-dimensional graphics and Mr. Russ Mueller for the scanning electron micrographs shown in this paper.

REFERENCES

1. Haynes, H. W., *Catal. Rev.-Sci. Eng.* **30**(4), 563 (1988).
2. Reyes, S. C., Iglesia, E., and Jensen, K. F., *Solid State Ionics* **32/33,** 833 (1989).
3. Satterfield, C. N., "Heterogeneous Catalysis in Practice." McGraw–Hill, New York, 1980.
4. Smith, J. M., "Chemical Engineering Kinetics." McGraw–Hill, New York, 1970.
5. Reyes, S. C., and Jensen, K. F., *Chem. Eng.Sci.* **40,** 1723 (1985).
6. Abbasi, M. H., Evans, J. W., and Abramson, I. S., *AIChE J.* **29**(4), 617 (1983).
7. Reyes, S. C., and Iglesia, E., *Chem. Eng. Sci.* **46**(4), 1089 (1991).
8. Pollard, W. G., and Present, R. D., *Phys. Rev.* **73**(7), 762 (1948).
9. Bosanquet, C. H., British TA Report BR-507, September 27, 1944.
10. Wang, C. T., and Smith, J. M., *AIChE J.* **29** 132 (1983).
11. Froment, G., and Bischoff, K. B., "Chemical Reactor Analysis and Design." Wiley, New York, 1979.
12. Feng, C., and Stewart, W. E., *Ind. Eng. Chem. Fundam.* **12** 143 (1973).
13. Zheng, L. H., and Chiew, Y. C., *J. Chem. Phys.* **90**(1), 322 (1989).
14. Huizenga, D. G., and Smith, D. M., *AIChE J.* **32**(1), 1 (1986).
15. Reyes, S. C., Duran, M. A., and Iglesia, E., *in* "Proceedings, 11th North American Catalysis Society Meeting," Dearborn, Michigan, 1989.
16. Boudart, M., de Menorval, L. C., Fraissard, J., and Valenca, G. P., *J. Phys. Chem.* **92,** 4033 (1988).